

Does the Fundamental Metallicity Relation evolve with redshift? A perspective from cosmological simulations

Alex M. Garcia¹^{*}, Paul Torrey¹, Lars Hernquist², Sara Ellison³, Lisa J. Kewley², Kathryn Grasha^{4,5,6}[†], Henry R.M. Zovaro⁴, Erica J. Nelson⁷, Z.S. Hemler⁸, Qian-Hui Chen^{4,5}

¹*Department of Astronomy, University of Virginia, Charlottesville, VA 22904, USA*

²*Institute for Theory and Computation, Harvard-Smithsonian Center for Astrophysics, Cambridge, MA 02138, USA*

³*Department of Physics & Astronomy, University of Victoria, Finnerty Road, Victoria, British Columbia, V8P 1A1, Canada*

⁴*Research School of Astronomy & Astrophysics, Australian National University, Canberra, Australia, 2611*

⁵*ARC Centre of Excellence for All Sky Astrophysics in 3 Dimensions (ASTRO 3D), Australia*

⁶*Visiting Fellow, Harvard-Smithsonian Center for Astrophysics, 60 Garden Street, Cambridge, MA 02138, USA*

⁷*Department for Astrophysical and Planetary Science, University of Colorado, Boulder, CO 80309, USA*

⁸*Department of Astrophysical Sciences, Princeton University, Peyton Hall, Princeton, NJ, 08544, USA*

Accepted XXX. Received YYY; in original form ZZZ

ABSTRACT

The scatter about the stellar mass gas-phase metallicity relation (MZR) correlates with the gas content of systems (indicated by, e.g., gas fraction or star formation rate). The lack of evidence of evolution in the correlated scatter at $z \lesssim 2.5$ leads many to refer to the relationship between mass, metallicity, and gas content as the Fundamental Metallicity Relation (FMR). Yet recent high-redshift *JWST* observations have challenged the fundamental nature of the FMR by showing that galaxies are offset from the locally defined FMR. In this work, we show that the cosmological simulations Illustris, IllustrisTNG, and EAGLE all predict non-negligible evolution of the FMR as a function of redshift. As a consequence, when fitting high- z galaxies with the low- z parameterisation, offsets are expected behaviour. We also show that when fitting galaxies at individual redshifts, opposed to assuming no redshift evolution, the scatter within the relationship decreases by an additional 10–30% at $z \gtrsim 4$, further suggesting evolution of the FMR.

Key words: galaxies: high-redshift – galaxies: abundances – galaxies: evolution

1 INTRODUCTION

The metal content of galaxies provides key insights into galaxy formation and evolution. Stellar winds and supernovae explosions eject metals formed in stars into the interstellar medium (ISM). Metals then mix via galactic winds (e.g., Lacey & Fall 1985; Koeppen 1994) and turbulence (e.g., Elmegreen 1999) within the disc while pristine gas accretion from the circumgalactic medium (CGM) dilutes the metal content (e.g., Somerville & Davé 2015). Thus, the metal content (metallicity) of the gas within a galaxy is sensitive to such interactions, providing a window into the evolutionary processes within a galaxy (Dalcanton 2007; Kewley et al. 2019).

Evidence for the sensitivity of metal content to the gas dynamics within a galaxy is perhaps most clearly seen within the relationship between the stellar mass of a galaxy and its gas-phase metallicity. This mass-metallicity relationship (MZR) describes a relationship of increasing metal content in galaxies with increasing stellar mass (Tremonti et al. 2004; Lee et al. 2006). While at the low stellar masses ($\log[M_*/M_\odot] \gtrsim 9.0$) this relationship is well-described as a power-law, at high masses ($\log[M_*/M_\odot] > 10.5$) the relationship plateaus

(e.g., Blanc et al. 2019). Furthermore, at a fixed stellar mass low (high) metallicity galaxies have systematically elevated (depressed) gas content (indicated by, e.g., gas fraction, star formation rate, or molecular gas mass; Ellison et al. 2008; Mannucci et al. 2010; Bothwell et al. 2013). The inverse relationship between a galaxy’s metal and gas content at a fixed stellar mass has been seen in observations for the gas-phase (e.g., Lara-López et al. 2010; Bothwell et al. 2016; Yang et al. 2022) and simulations for both the gas-phase (e.g., De Rossi et al. 2017; Torrey et al. 2018) and stellar metallicities (De Rossi et al. 2018; Fontanot et al. 2021; Garcia et al. Prep). This correlated scatter about the MZR is qualitatively well-described with basic competing physical drivers: (i) as new (low metallicity) gas is accreted onto a galaxy, it drives galaxies toward higher gas fractions, higher star formation rates (SFRs), and lower metallicities, while (ii) galaxies will persistently tend to consume gas and produce new metals, driving them toward lower gas fractions, lower SFRs, and higher metallicities (Torrey et al. 2018). It is therefore expected that correlated scatter would remain present for galaxies across a wide redshift range given the ubiquity of these physical drivers.

At higher redshift the MZR has been seen to persist (albeit with a lowered overall normalisation e.g., Savaglio et al. 2005; Maiolino et al. 2008; Zahid et al. 2011; Langeroodi et al. 2022) along with correlated scatter about the MZR (e.g., Belli et al. 2013; Salim et al.

^{*} E-mail: alexgarcia@virginia.edu

[†] ARC DECRA Fellow

2015; Sanders et al. 2018, 2021). Critically, it has been put forth that a single, redshift-invariant plane can be used to describe both the general evolution of the MZR as well as the residual correlations about it (Mannucci et al. 2010). This single surface/relation that can describe the metallicity of galaxies over a wide mass and redshift range is referred to as the fundamental metallicity relation (FMR) – where its “fundamental” nature is usually tied to its redshift invariance.

The FMR is typically parameterised via quantifying the relationship between stellar mass, gas-phase metallicity, and SFR ($M_* - Z_{\text{gas}} - \text{SFR}$) at $z \approx 0$ using large surveys of local galaxy populations (such as the Sloan Digital Sky Survey Abazajian et al., 2009; see, e.g., Mannucci et al. 2010). The $z = 0$ calibrated FMR is then extrapolated to higher redshift galaxy populations (e.g., Salim et al. 2015; Cresci et al. 2019; Sanders et al. 2021). A number of studies have found that in extrapolating past $z = 0$ galaxies cluster reasonably around a single, redshift-invariant FMR (out to redshift $z \approx 2-3$ Mannucci et al. 2010; Cresci et al. 2019). At $z \sim 3$, however, galaxies start to appear to be systematically metal poor compared to low redshift predictions (Troncoso et al. 2014; Onodera et al. 2016). Recent *JWST* observations have corroborated high redshift offsets in showing that past $z \gtrsim 5$ galaxies are even more metal poor compared to low redshift FMR predictions (Heintz et al. 2022; Curti et al. 2023; Langeroodi & Hjorth 2023; Nakajima et al. 2023). As such, the redshift-invariance of the FMR has come into question in recent years, with some suggesting the the FMR is instead a state of equilibrium not achieved by galaxies until $z \sim 3$ (Heintz et al. 2022; Langeroodi & Hjorth 2023).

The core challenge of the FMR is that it aims to characterise two distinct features of the MZR at the same time: (i) the residual correlation with gas content, and (ii) the redshift evolution of the normalisation. It is therefore possible that a change in either the strength of the residual correlation or the redshift evolution of the MZR (or a combination thereof) can indicate FMR evolution. Yet, it is presently unclear how to effectively decouple and interpret evolution in either or both of the two features. This gives rise to the question: How do we identify (and subsequently interpret) deviations from the FMR? In this work, we offer predictions for the FMR from the perspective of cosmological simulations to address that question.

The rest of paper is as follows: In §2 we describe the simulations we use, our galaxy selection criteria, and introduce a framework for interpreting the Mannucci et al. (2010) parameterisation of the FMR. In §3, we summarize definitions of the FMR. In §4 we present the redshift evolution of the FMR as found in simulations, examine how well a $z = 0$ calibrated FMR does at high redshift, and make comparisons to recent *JWST* observations. In §5 we quantify the impact of the new framework on the scatter about the MZR, consider a slight modification within the framework, and offer insight on how to evaluate each relationship presented. Finally, in §6 we present our conclusions.

2 METHODS

We use the Illustris, IllustrisTNG, and EAGLE cosmological simulations to investigate the dependence of the gas-phase metallicity on stellar mass and star formation. Each of these simulations has a sub-grid ISM pressurisation model, which manifestly creates “smooth” stellar feedback. We believe that generic results from all three of these simulations should constitute a fair sampling of predictions from sub-grid ISM pressurisation models owing to the appreciably different physical implementations.

Here we briefly describe each of the simulations from this analysis,

the galaxy selection criteria we employ, and present a new framework for interpreting the Mannucci et al. (2010; hereafter M10) FMR projection. All measurements are reported in physical units. Many of the methods here follow from Garcia et al. (Prep).

2.1 Illustris

The original Illustris suite of cosmological simulations (Vogelsberger et al. 2013, 2014a,b; Genel et al. 2014; Torrey et al. 2014) was run with the moving-mesh code AREPO (Springel 2010). The Illustris model accounts for many important astrophysical processes, including gravity, hydrodynamics, star formation/stellar evolution, chemical enrichment, radiative cooling and heating of the ISM, stellar feedback, black hole growth, and AGN feedback. The unresolved star forming ISM uses the Springel & Hernquist (2003; hereafter, SH03) equation of state, wherein new star particles are created from regions of dense ($n_{\text{H}} > 0.13 \text{ cm}^{-3}$) gas. The masses of the stars within the star particle are drawn from a Chabrier (2003) initial mass function (IMF) and metallicities are adopted from the ISM where they are born. As the stars evolve, they eventually return their mass and metals back into the ISM. The stellar mass return and yields used allow for the direct simulation of time-dependent return and heavy metal enrichment, explicitly tracking nine different chemical species (H, He, C, N, O, Ne, Mg, Si, and Fe).

The Illustris suite consists of a single volume of size $(106.5 \text{ Mpc})^3$ at three different resolutions. The three resolutions are as follows: Illustris-1 (2×1820^3 particles), Illustris-2 (2×910^3 particles), and Illustris-3 (2×455^3 particles). We use Illustris-1, the highest resolution run, which is hereafter we refer to synonymously with Illustris itself.

2.2 IllustrisTNG

IllustrisTNG (The Next Generation; Marinacci et al. 2018; Naiman et al. 2018; Nelson et al. 2018; Pillepich et al. 2018b; Springel et al. 2018; Pillepich et al. 2019; Nelson et al. 2019a,b, hereafter TNG) is the successor to the original Illustris simulations, alleviating some of the deficiencies of and updating the original Illustris model. As such, the Illustris and TNG models are similar, yet have an appreciably different physical implementation (see Weinberger et al. 2017; Pillepich et al. 2018a, for a complete list of differences between the models). TNG implements the same equation of state for the dense star forming ISM as Illustris (SH03). Furthermore, TNG tracks the same nine chemical species as Illustris, while also following a tenth “other metals” as a proxy for metals not explicitly monitored.

TNG consists of three different volumes each with their own sub-resolution runs: TNG50 ($51.7 \text{ Mpc})^3$, TNG100 ($110.7 \text{ Mpc})^3$, and TNG300 ($302.6 \text{ Mpc})^3$. In this work, we will use the highest resolution TNG100 run (TNG100-1; hereafter used synonymously with TNG), with 2×1820^3 particles, as a comparable volume and resolution to the original Illustris.

2.3 EAGLE

Unlike Illustris and TNG, “Evolution and Assembly of GaLaxies and their Environment” (EAGLE, Crain et al. 2015; Schaye et al. 2015; McAlpine et al. 2016) employs a heavily modified version of the smoothed particle hydrodynamics (SPH) code GADGET-3 (Springel 2005; ANARCHY, see Schaye et al. 2015 Appendix A). EAGLE includes many of the same baryonic processes (star-formation, chemical enrichment, radiative cooling and heating, etc) as Illustris and

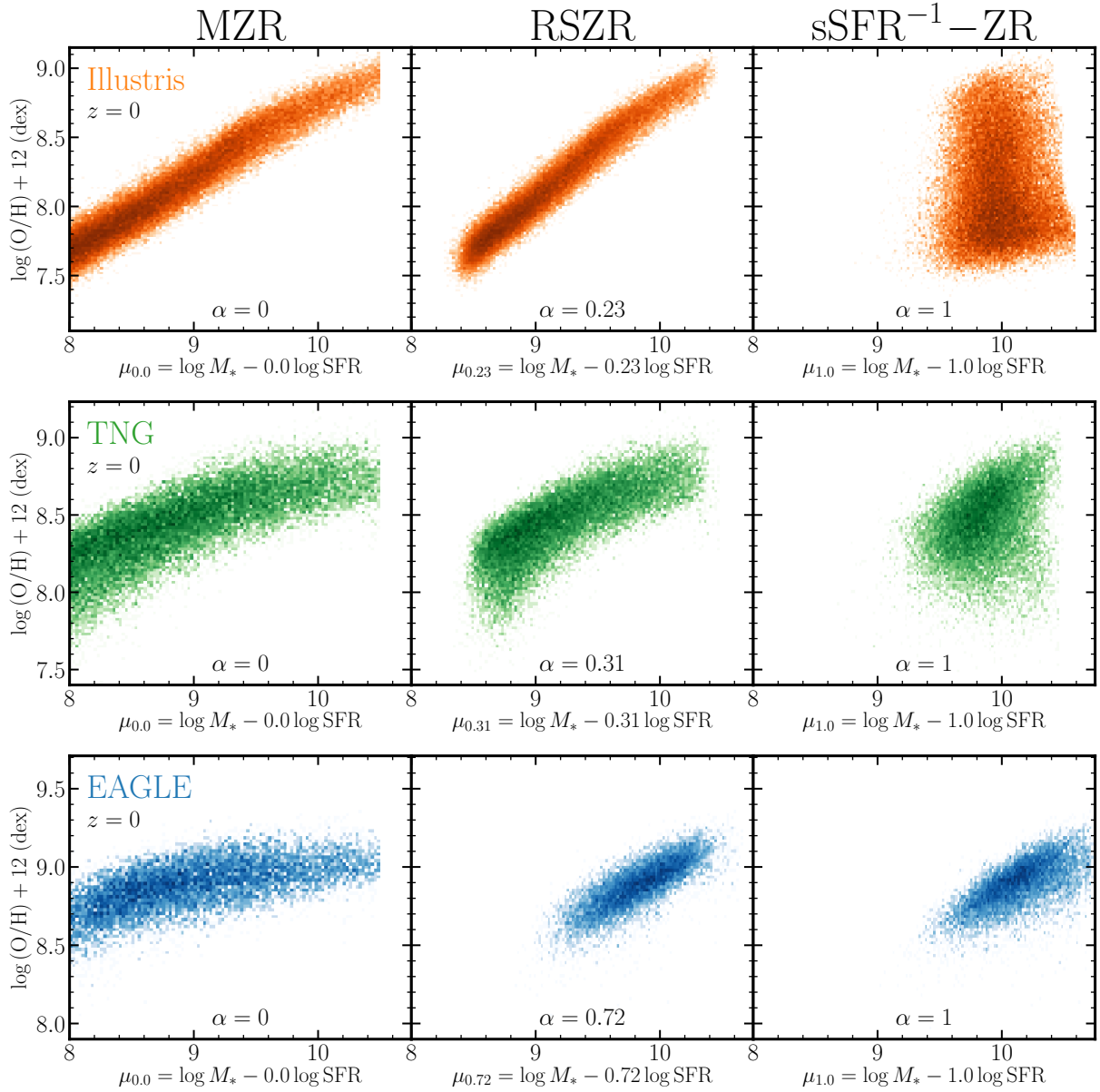


Figure 1. Three important regimes of the μ_α ZR at $z = 0$ in Illustris, TNG, and EAGLE. *Left Column:* the stellar mass gas-phase metallicity relation (MZR) which corresponds to $\alpha = 0.0$, *Middle Column:* the reduced scatter metallicity relation (RSZR) which corresponds to the α value that minimizes the scatter in these relations (α_{\min}), and *Right Column:* the inverse specific star formation rate gas-phase metallicity relation (sSFR $^{-1}$ -ZR) which corresponds to $\alpha = 1.0$, all for star forming galaxies in Illustris, TNG, and EAGLE at $z = 0$ (top, middle, bottom, respectively). Note that the ordinate axes from row-to-row are on different scales.

TNG. The dense (unresolved) ISM in EAGLE is also treated with a sub-grid equation of state (Schaye & Dalla Vecchia 2008; hereafter, SDV08), much like that of SH03. The SDV08 prescription forms stars according to a Chabrier (2003) IMF from the dense ISM gas. The density threshold for star formation is given by the metallicity-dependent transition from atomic to molecular gas computed by Schaye (2004). Stellar populations evolve according to the Wiersma et al. (2009) evolutionary model and eventually return their mass and metals back into the ISM. EAGLE explicitly tracks eleven different chemical species (H, He, C, N, O, Ne, Mg, Si, S, Ca, and Fe).

The full EAGLE suite is comprised of several simulations ranging

from size $(25 \text{ Mpc})^3$ to $(100 \text{ Mpc})^3$. We use data products at an intermediate resolution $(2 \times 1504^3 \text{ particles})$ run with a box-size of $(100 \text{ Mpc})^3$ referred to as REFLO100N1504 (hereafter simply EAGLE) as a fair comparison to the selected Illustris and TNG runs.

2.4 Galaxy Selection

All three simulations in this work select gravitationally-bound substructures using SUBFIND (Springel et al. 2001; Dolag et al. 2009), which identifies self-bound collections of particles from within friends-of-friends groups (Davis et al. 1985). We limit our analy-

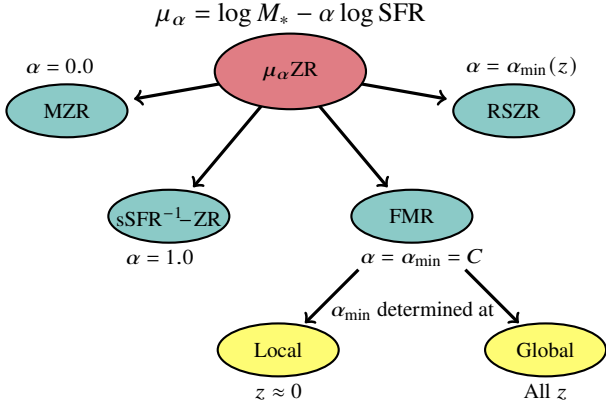


Figure 2. Decision tree for the μ_α ZR, see Section 3.1 for full details. This shows the relationship between four different metallicity parameterisations that can be included under the umbrella μ_α metallicity relation (μ_α ZR; see Equation 1): (i) the traditional MZR which is $\alpha = 0.0$, (ii) an inverse specific star formation rate metallicity relation (sSFR⁻¹-ZR) where $\alpha = 1.0$, (iii) the FMR where $\alpha = \alpha_{\min}$ and is constant as a function of redshift, and (iv) the reduced scatter metallicity relation (RSZR) where $\alpha = \alpha_{\min}$ but α_{\min} is allowed to vary as a function of redshift. Moreover, the FMR can be further broken into two categories: calibrated only at $z \approx 0$ (local FMR) or at all z (global FMR).

sis to central galaxies that we consider ‘well-resolved’ (i.e., containing ~ 100 star particles and ~ 500 gas particles), thus we restrict the sample to galaxies with stellar mass $\log(M_* [M_\odot]) > 8.0$ and gas mass $\log(M_{\text{gas}} [M_\odot]) > 8.5$. To limit the impact of AGN on our galaxy sample we omit galaxies with stellar mass greater than $\log(M_* [M_\odot]) > 10.5$. Following from a number of previous works (see, e.g., Donnari et al. 2019; Nelson et al. 2021; Hemler et al. 2021; Garcia et al. 2023), we exclude quiescent galaxies by defining a specific star formation main sequence (sSFMS). We do so by fitting a linear-least squares regression to the median sSFR- M_* relation with stellar mass $\log(M_* [M_\odot]) < 10.2$ in mass bins of 0.2 dex. The sSFMS above $10.2 \log M_\odot$ is extrapolated from the regression. Galaxies that fall greater than 0.5 dex below the sSFMS are not included in our sample. As we show in Garcia et al. (Prep; that paper’s Appendix B) our key results (using stellar metallicities) are *not* sensitive to our sample selection. We obtain the same result here in the gas-phase: our key results are qualitatively unchanged by the same variations as Garcia et al. (Prep) in selection criteria.

3 DEFINITIONS OF THE FMR

3.1 The μ_α Metallicity Relation

M10 project the 3D relationship between stellar mass, gas-phase metallicity, and star formation rate (SFR) into 2D using a linear combination of the stellar mass and star formation:

$$\mu_\alpha = \log M_* - \alpha \log \text{SFR}, \quad (1)$$

where α is a free parameter that ranges from 0 to 1. The free parameter α holds all the diagnostic power on the strength of the MZR’s residual correlation with SFR in this projection. By varying α , the distribution of galaxies in μ_α -metallicity space varies. We define a μ_α -metallicity relation (μ_α ZR) for each α as a linear-least squares regression¹ of the

data. We compute the μ_α ZR for $\alpha = 0.0$ to 1.0 in steps of 0.01 and obtain the residuals about each regression. The projection that yields the minimum scatter (smallest standard deviation) in the residuals is deemed the best fit. The α value associated with this minimum scatter projection is henceforth referred to as α_{\min} . By assuming that a projection that has scatter within 5% of the minimum scatter projection is a plausible candidate for the true α_{\min} , we define an uncertainty on α_{\min} (following from Garcia et al. Prep).

The μ_α ZR is the relation of merit in the 2D projection. Three interesting regimes of the μ_α ZR naturally arise: (i) $\alpha = 0.0$, wherein the canonical MZR is recovered (left column panels of Figure 1), (ii) $\alpha = 1.0$, wherein an inverse specific star formation rate-metallicity relation (sSFR⁻¹-ZR; right column panels of Figure 1) is obtained, and (iii) $\alpha = \alpha_{\min}$, wherein the scatter about the relation is minimized (middle column panels of Figure 1).

Traditionally (as in, e.g., M10), the FMR is defined by fitting for α_{\min} at $z = 0$ and assuming the derived α_{\min} to be a constant as a function of redshift. This need not be the case. We relax the assumption that α_{\min} is constant over time by identifying the α_{\min} value that minimizes scatter at each redshift independently, allowing α_{\min} to (potentially) vary as a function of redshift. We designate the μ_α projection where the scatter is minimized at each redshift independently as the ‘reduced scatter metallicity relation’ (RSZR) to differentiate from the traditional FMR. If we instead enforce the condition that α_{\min} is a constant as a function of redshift, we obtain the traditional FMR. The traditional FMR’s α_{\min} can be determined either using all galaxies across redshift (globally) or at $z = 0$ (locally; as in observations fitting with SDSS data). We restrict our analysis of the FMR to the local (i.e., $z = 0$ parameterised) FMR as a fair comparison to observations.

The μ_α ZR can be thought of as a superset of relations containing the MZR, RSZR, global FMR, local FMR, and sSFR⁻¹-ZR (relationships illustrated in Figure 2). Framing the FMR in this way underscores the large number of decisions required in establishing the FMR. Previous studies have been somewhat restrictive in regards to these decisions (i.e., focusing primarily on the local FMR). We therefore highlight the need to take a deliberate approach to our definitions to build a framework by which potential redshift evolution can be assessed. To that end, careful consideration is placed in specifying what is an FMR (local and global FMRs) and what is *not* an FMR (RSZR).

3.2 Strong and Weak FMR Hypotheses

Physically, α_{\min} sets the direction to project the 3D $M_* - Z_{\text{gas}} - \text{SFR}$ space into a minimum scatter distribution in 2D $\mu_\alpha - Z$ space. The central question of the FMR investigation in the M10 framework is: Can the 2D projection explain both: (i) the scatter about the MZR, and (ii) the evolution of normalisation in the MZR through time. We henceforth refer to the idea that a 2D projection *can* describe both with the single parameter α_{\min} as the strong FMR hypothesis.

It is possible that the M10 projection simply does not satisfy the strong FMR hypothesis. Perhaps the evolution of scatter and normalisation are disjoint – or at least not the same. The idea of an FMR need not be abandoned in this case. We define a weak FMR hypothesis as the projection direction remaining the same at each redshift (α_{\min} same at all redshifts). In the weak FMR hypothesis

¹ M10 use a fourth-order polynomial for fitting. This practice is inconsistent in the literature with many (e.g., Andrews & Martini 2013) considering a

linear regression. We show that using a fourth-order polynomial instead of a linear regression does not significantly alter our α_{\min} determination in Appendix A.

	Illustris	TNG	EAGLE
$z = 0^\dagger$	$0.23^{0.33}_{0.10}$	$0.31^{0.57}_{0.00}$	$0.72^{0.84}_{0.56}$
$z = 1$	$0.32^{0.45}_{0.13}$	$0.61^{0.68}_{0.49}$	$0.73^{0.81}_{0.63}$
$z = 2$	$0.39^{0.52}_{0.21}$	$0.59^{0.67}_{0.48}$	$0.65^{0.75}_{0.52}$
$z = 3$	$0.45^{0.56}_{0.30}$	$0.65^{0.71}_{0.55}$	$0.59^{0.68}_{0.45}$
$z = 4$	$0.48^{0.58}_{0.36}$	$0.68^{0.75}_{0.57}$	$0.53^{0.62}_{0.39}$
$z = 5$	$0.52^{0.61}_{0.39}$	$0.70^{0.77}_{0.59}$	$0.46^{0.56}_{0.33}$
$z = 6$	$0.53^{0.63}_{0.39}$	$0.70^{0.77}_{0.59}$	$0.44^{0.54}_{0.31}$
$z = 7$	$0.56^{0.65}_{0.42}$	$0.70^{0.78}_{0.58}$	$0.40^{0.49}_{0.27}$
$z = 8$	$0.59^{0.69}_{0.47}$	$0.70^{0.78}_{0.58}$	$0.31^{0.42}_{0.16}$

Table 1. All α_{RSZR} values at $z = 0 - 8$ for Illustris, TNG, and EAGLE. At each redshift the α_{min} values are determined by using the RSZR (see Sections 3 and 4.1. The superscripts are the upper limits of the uncertainty while the subscripts are the lower limits. We show these values in Figure 3. † The $z = 0$ values are also α_{local} .

the evolution of the normalisation is *not* driven by the same physical mechanism as the evolution of scatter about it. The physics driving the scatter, however, is consistent across all redshifts.

Models with more complexity than a linear combination of parameters may be required to fully characterise the $M_* - Z_{\text{gas}} - \text{SFR}$ relationship. Models exist at present with more complexity; for example, Curti et al. (2020) introduce a functional form for the FMR (opposed to a 2D projection). We opt to not present other forms of the FMR in this work as an exercise on the extent to which the M10 projection can describe both the evolution of scatter and normalisation of the MZR.

3.3 Parameters of the FMR and RSZR

We further clarify that α_{min} values determined in the RSZR are α_{RSZR} , local FMR are α_{local} , and using the global FMR are α_{global} . There are nine α_{RSZR} values ($z = 0-8$) since we allow it to vary and one of α_{local} and α_{global} by construction of an FMR. We note that α_{local} and α_{global} values may be the same if the correlated scatter about the MZR does not change from that of $z = 0$. α_{global} values, however, have some intrinsic dependence on the evolution of the normalisation of the MZR. As such, α_{global} may deviate from the α_{local} , even if the correlated scatter does not evolve with redshift.

There are two more parameters beyond α_{min} that the $\mu_{\alpha\text{ZR}}$ is defined by: the slope and intercept of the regression. These additional parameters add complexity to the interpretation of the evolution. For the RSZR, the slope and intercept at each redshift may vary even if α_{min} does not. Similarly, the regression of the local FMR may not match that of the global FMR even if the α_{min} values do. Regressions are inherently linked to the α_{min} determination, yet the parameters of the fit can have a profound impact on interpretation of FMR evolution irrespective of α_{min} variations.

4 RESULTS

We define FMR invariance as implying: (i) the correlated scatter about the MZR does not vary as a function of redshift, and (ii) the plane on which the $z = 0$ galaxies falls is the same as that of higher redshift galaxies. We consider each claim separately to investigate whether both statements hold. First, we probe the variations of the scatter about the MZR by characterising it at each individual redshift.

Then we examine if the local FMR can capture behaviour at higher redshifts by way of an investigation of offsets from the regression.

4.1 Does α_{RSZR} vary as a function of redshift?

We use the RSZR – and specifically the best-fit α_{min} values derived as a function of redshift – to evaluate whether the properties of the residual scatter about the MZR evolve significantly with redshift. The RSZR is well suited for this purpose because it fits each redshift independently, and is therefore not sensitive to the influence of redshift evolution of the normalisation of the MZR. As such, the RSZR is an effective tool for assessing if/how the scatter about the MZR changes with time.

We obtain α_{RSZR} values at $z = 0 - 8$ by fitting the RSZR at each redshift for all three simulations (shown in Figure 3; values presented in Table 1). Uncertainties on α_{RSZR} correspond to the uncertainty in the determined minimum dispersion (see Section 3 for definition). α_{RSZR} values show some level of redshift evolution in all three simulations as can clearly be seen from Figure 3. Interestingly, each simulation has qualitatively different behaviour. α_{RSZR} values show weak signs of increasing with increasing redshift at low redshift but plateau past $z \gtrsim 2$ in TNG. Illustris α_{RSZR} values increase monotonically with redshift, while the EAGLE values decrease monotonically as a function of redshift.

No statements on the strong FMR hypothesis (evolution of scatter and normalisation are driven by same mechanisms) can be made from α_{RSZR} variations since the RSZR removes all dependence of the evolution of the normalisation of the MZR. The weak FMR hypothesis, however, is probed directly by testing α_{RSZR} variations. The evolution in α_{RSZR} implies that the weak FMR hypothesis is not satisfied in any of the three simulations. Redshift evolution of the derived α_{RSZR} values is therefore indicative of evolution in the driving forces of the scatter about MZR (potentially ramping up or down with time in the case of Illustris and EAGLE). For example, barring $z = 0$, all α_{RSZR} values from TNG agree within uncertainty. As was shown in Garcia et al. (Prep), a $M_* - Z_* - \text{SFR}^2$ relation is not apparent at low mass in TNG at $z = 0$. Garcia et al. (Prep) attribute this lack of a relationship at $z = 0$ in TNG to the redshift scaling of winds within the TNG model. Briefly, the effect of adding winds that change with redshift suppresses low redshift star formation and increases the efficacy of high redshift stellar feedback compared to the Illustris model (see Pillepich et al. 2018a). It is therefore likely that the suppressed low redshift star formation causes the downturn of α_{min} values at low- z as well as the large uncertainty on α_{min} at $z = 0$. The lack of evolution in α_{RSZR} at higher redshifts may be a feature of the increased efficacy of stellar feedback at these higher redshifts. As such, features of α_{RSZR} are likely sensitive to details of the wind implementation/strength prescribed by the model on which it is built.

Our result in EAGLE indicating significant redshift evolution seemingly contradicts a previous study finding the FMR is in place and does not evolve out to $z \approx 5$ in EAGLE (De Rossi et al. 2017). There is a subtle difference in the analysis between the two works,

² While we show in Garcia et al. (Prep) this for the *stellar* metallicities, we also show in that paper that stellar and gas-phase metallicities are proportional to each other in TNG (see Section 4.1 of that work). Therefore, the same physical mechanism suppressing the correlated scatter for stellar metallicities is likely what is suppressing α_{min} for the gas-phase as well. We note, however, that it is probable that the causality is in the opposite direction as described above.

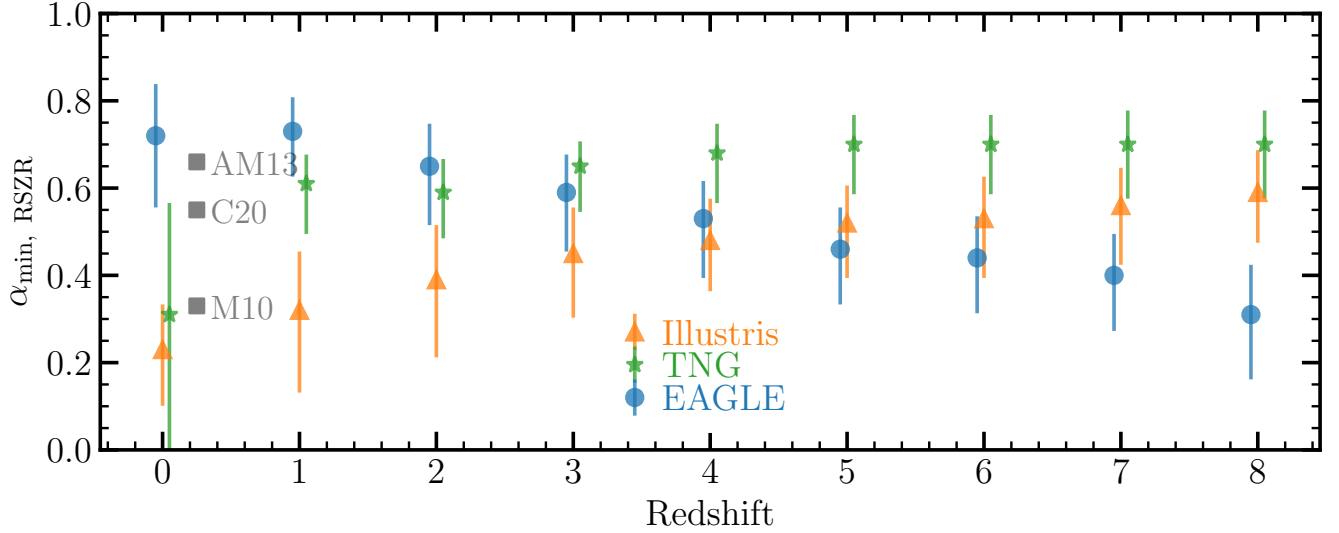


Figure 3. α_{RSZR} values as a function of redshift in Illustris, TNG, and EAGLE. The RSZR α_{\min} values as a function of redshift are plotted as orange triangles, green stars, and blue circles for Illustris, TNG, and EAGLE, respectively. The errorbars here are obtained by finding α values that reduce the scatter to within 5% that of the minimized scatter. The gray squares are observational values of α_{\min} from M10, Andrews & Martini (2013), and Curti et al. (2020) determined at $z \approx 0$ via SDSS (offset from $z = 0$ for aesthetic purposes).

however: De Rossi et al. (2017) do not parameterise the FMR to test α_{RSZR} variations. They qualitatively examine the residual correlation within the MZR and show that a $M_* - Z_{\text{gas}} - \text{SFR}$ relation exists at $z = 0 - 5$. This is in agreement with our results here. Consistent with De Rossi et al. (2017), we find that an $M_* - Z_{\text{gas}} - \text{SFR}$ relation at $z = 0 - 5$ exists in EAGLE via non-zero alpha values. Despite the persistence of the $M_* - Z_{\text{gas}} - \text{SFR}$ relation, we find that there is some evolution through $z = 0 - 5$ in EAGLE by using the M10 projection of the FMR. It should be noted that the uncertainty of the $z = 0$ and $z = 5$ values do overlap in EAGLE. The subtlety of the redshift evolution may therefore be difficult to detect without specifically using the RSZR (or equivalent relationship).

Overplotted on Figure 3 (gray squares) are three observationally determined values of α_{\min} from M10 (0.33), Andrews & Martini (2013; 0.66), and Curti et al. (2020; 0.55). Each of these values was determined using SDSS galaxies at $z \approx 0$. The M10 α_{\min} value agrees fairly well with the TNG derived value at $z = 0$, although the uncertainty on the TNG α_{\min} is significant enough to include the Curti et al. (2020) value by a factor of ~ 1.5 times higher. Similarly, the Andrews & Martini (2013) value of 0.66 agrees fairly well with the derived value from EAGLE at $z = 0$.

4.2 Implications of using a fixed α_{\min}

In the previous sub-section, we considered if a single alpha value could adequately describe the nature of the correlated scatter across different redshift bins. We now consider the implications of using a single, fixed alpha. There are two different values one could consider keeping α_{\min} fixed at: α_{local} (the $z = 0$ calibrated value) or α_{global} (includes galaxies across the entire redshift range). We use the locally derived FMR, wherein α_{\min} and the FMR regression are determined at $z = 0$, as a fair comparison to observations.

Figure 4 shows the local FMR for EAGLE (Illustris and TNG versions of this Figure available in Appendix B). The large left panel shows the FMR applied across all redshifts with the solid black

line being the best fit regression about which the $z = 0$ scatter is minimized³. Each of the nine panels on the right show each individual redshift's galaxy population against the local FMR. We find that the α_{local} values for Illustris, TNG, and EAGLE are 0.23, 0.31, and 0.72 (respectively; also shown in Table 1).

The $z = 0$ regression passes through the distribution of galaxy data points without any significant bias in each of the three simulations at low redshifts ($z \lesssim 1 - 2$). However, past $z \gtrsim 2 - 3$, there are clear systematic offsets in the metallicity of galaxy populations compared to the $z = 0$ regression. In EAGLE, for example, most of the galaxies at $z = 8$ are ~ 0.5 dex offset from the local FMR regression. Interestingly, the redshift range of lack of offsets falls roughly in line with observations that claim the FMR does not evolve until $z \sim 3$ (e.g., Onodera et al. 2016; Sanders et al. 2018; Cresci et al. 2019). This agreement with observations indicates a tension with the concept of a redshift-invariant FMR. The local FMR is evidently not a perfect descriptor of metallicity evolution before $z \sim 3$.

High redshift offsets indicate that there are not one, but two metrics by which one can assess the quality of the local FMR fit. The first metric (discussed in the previous section) is variations in the derived α_{RSZR} values. The second is how well the regression captures redshift evolution of the normalization of the MZR (i.e., existence of offsets). Offsets from the local FMR are quantitatively examined in the following section.

4.2.1 High redshift offsets from the local FMR

We obtain offsets via residuals from the local FMR regression extrapolated at each redshift (as in Figure 4). The convention of negative offsets implying more metal poor than FMR predictions is adopted here from observational studies. Figure 5 shows the residuals from

³ It should be noted that the local FMR regression is identical to that of the $z = 0$ RSZR, but now we apply it across redshift bins. We consider a modification to this prescription in Section 5.1.2.

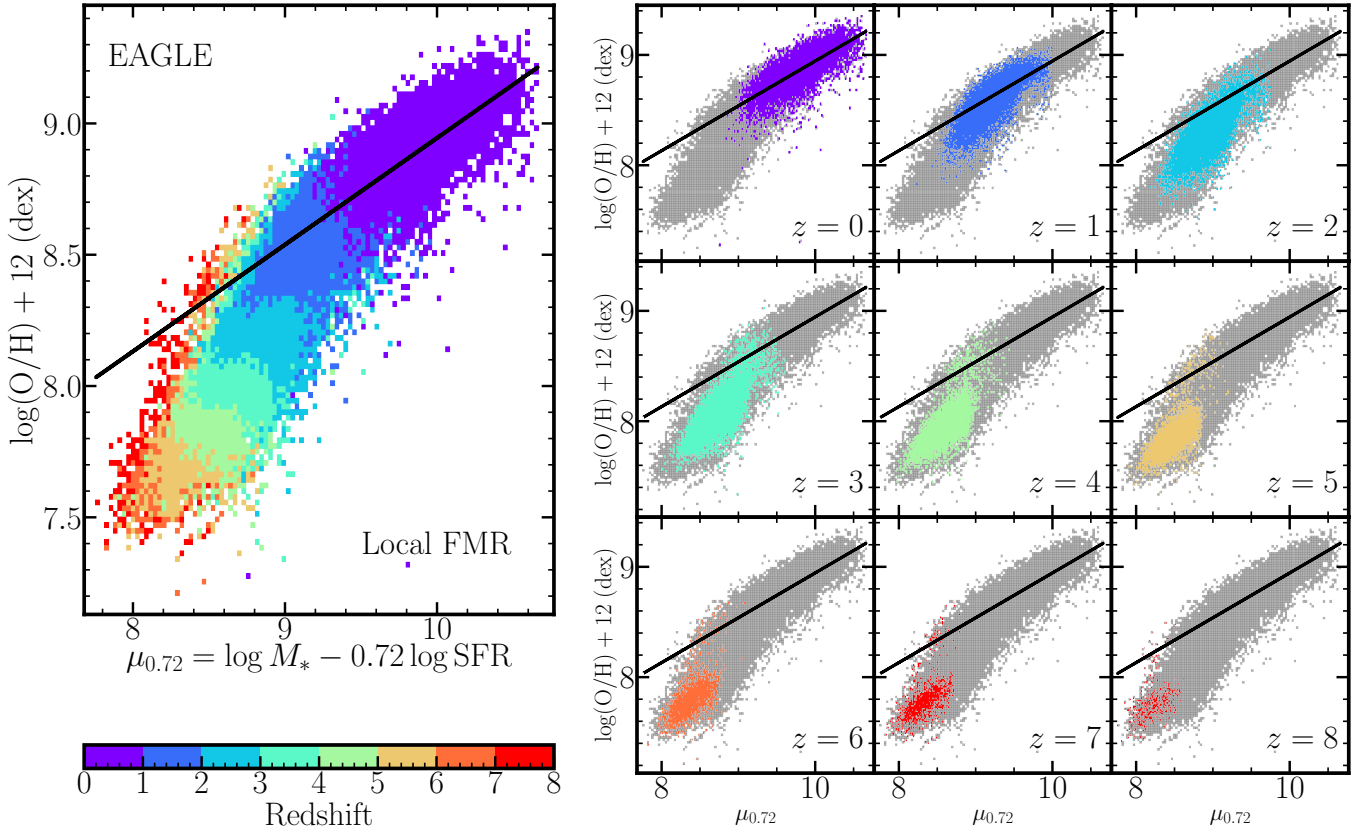


Figure 4. The local FMR (fit at $z = 0$ and applied to all galaxies $z = 0 - 8$) for EAGLE. *Left:* The local FMR for EAGLE $z = 0 - 8$, each pixel corresponds to the average redshift in that bin with ‘bluer’ pixels being low redshift and ‘redder’ pixels being high redshift. The black line is the regression line about which the scatter (at $z = 0$) is determined. *Right:* Local FMR fit now for the galaxy populations at each individual redshift from $z = 0$ to $z = 8$ with the full galaxy population as a gray background. The black lines in each of these panels are the same black line in the large left panel.

the local FMR as a function of redshift for Illustris, TNG, and EAGLE. All of the residuals are centered around zero at $z = 0$ by construction. Residuals are systematically offset from zero with increasing redshift in each of the three simulations. Offsets become more negative with increasing redshift in TNG and EAGLE. Conversely, the offsets become more positive with increasing redshift in Illustris (high-redshift galaxies are systematically more *metal rich* compared to predictions). We compare the offsets in the simulations to summary statistics of recent high redshift observations provided by Langeroodi & Hjorth (2023; pink triangles), Curti et al. (2023; purple squares), and Nakajima et al. (2023; gold stars and dark blue circles⁴) in Figure 5. The magnitude of the offsets in observations is, on aggregate, larger than those we find in Illustris. Strikingly, the negative offsets of TNG and EAGLE are within the errorbars of Curti et al. (2023), Langeroodi & Hjorth (2023), and Nakajima et al. (2023, comparisons to Curti et al. 2020). It should be noted, however, that Nakajima et al. (2023, comparisons to Andrews & Martini 2013; the preferred comparison in that work) do not significantly deviate from 0.0 until past $z \sim 8$, much later than what simulations predict.

⁴ Nakajima et al. (2023) compares to both Curti et al. 2020 and Andrews & Martini 2013 FMR parameterisations (gold stars and dark blue circles in Figure 5, respectively) as a point of reference. However, Nakajima et al. prefer the comparison to Andrews & Martini as it probes a wider μ_α space.

5 DISCUSSION

5.1 Evaluating the redshift invariance of the FMR

As mentioned previously, there are two metrics by which FMR evolution can be evaluated: (i) variations in α_{RSZR} values, and (ii) offsets from the regression. Each metric holds different insights for interpreting potential redshift evolution of the FMR. The presence of variations in α_{min} indicates that the scatter within the MZR varies with time. Changes in the regression (i.e., slope/intercept), on the other hand, signal that the local FMR does not characterise galaxies at all redshifts.

We first consider the scatter about the local FMR compared to that of the MZR and RSZR in Section 5.1.1 to test how well the local FMR reduces scatter. Then we consider a modification to the local FMR by taking into account high-redshift galaxies to alleviate offsets in Section 5.1.2.

5.1.1 Implications of α_{RSZR} variations

Figure 6 illustrates three different ratios we examine to assess scatter reduction efficacy. We consider the RSZR fit does compared to the MZR as a baseline. The left panel of Figure 6 shows the standard deviation of the residuals about the RSZR normalised by that of the MZR as a function of redshift ($\sigma_{\text{RSZR}}/\sigma_{\text{MZR}}$). We find for all redshifts across the three simulations that the RSZR reduces the scatter by $\sim 10 - 30\%$ compared to the MZR. The exception is TNG

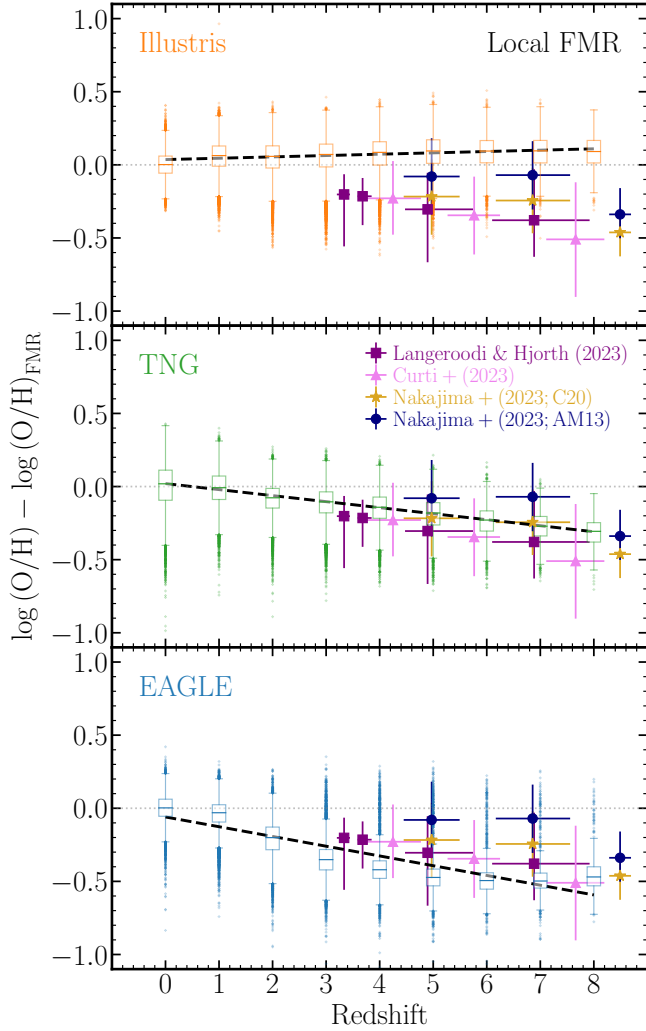


Figure 5. How do local FMR offsets in the simulations compare to observed high- z FMR offsets? Offsets from the FMR at all redshifts based on the $z = 0$ fit. The boxplots are the distribution of offsets from the simulation in each panel (Illustris, TNG, EAGLE are top, middle, and bottom, respectively) at each redshift. The black dashed line is a best fit through the medians. The purple squares and pink triangles are observational data from Langeroodi & Hjorth (2023) and Curti et al. (2023), respectively. The gold stars and dark blue circles are from Nakajima et al. (2023). The difference between the two Nakajima et al. (2023) points is the underlying FMR compared against: gold compares to Curti et al. (2020; $\alpha_{\min} = 0.55$) and dark blue compares to Andrews & Martini (2013; $\alpha_{\min} = 0.66$).

at $z = 0$ having scatter reduction of less than 5% – falling within the nominal uncertainty on α_{\min} and implying there is functionally no difference between the scatter of the MZR and RSZR at this redshift. $z = 0$ was discussed previously in the context of the α_{\min} value at this redshift in TNG (Section 4.1) and the lack of a relation was attributed to the redshift scaling winds in the TNG model (see Pillepich et al. 2018a). The scatter reduction is roughly constant as a function of redshift in both TNG and EAGLE at around $\sim 20\%$ (barring the aforementioned TNG exception). Scatter reduction in Illustris ranges from 10% at $z = 0$ to nearly 30% at $z = 8$.

Next, we examine the scatter about the local FMR fit evaluated at each redshift compared to that of the MZR at that redshift ($\sigma_{\text{LFMR}}/\sigma_{\text{MZR}}$; middle panel Figure 6). We find a similar trend to

that of $\sigma_{\text{RSZR}}/\sigma_{\text{MZR}}$: a roughly constant scatter reduction as a function of redshift in TNG, albeit at a reduced value of $\sim 5 - 10\%$ (see previous discussion about the exception at $z = 0$). The scatter reduction in Illustris is similarly constant around 10%. Evidently, the redshift evolution in Illustris seen previously with $\sigma_{\text{RSZR}}/\sigma_{\text{MZR}}$ disappears when using the local FMR fit. $\sigma_{\text{LFMR}}/\sigma_{\text{MZR}}$ actually *increases* nearly monotonically in EAGLE as a function of redshift: the local FMR fits the low redshift bins significantly better than the highest redshifts. Remarkably, the locally derived FMR actually begins to increase the scatter about the $\mu_{\alpha\text{ZR}}$ by 10 – 40% compared to the MZR at high redshift ($z > 5$) in EAGLE.

Finally, we show the ratio of the scatter about the RSZR divided by the scatter about the local FMR evaluated at each redshift ($\sigma_{\text{RSZR}}/\sigma_{\text{LFMR}}$; right panel of Figure 6). The ratio $\sigma_{\text{RSZR}}/\sigma_{\text{LFMR}}$ is of particular interest as it provides a diagnostic for how well the local FMR characterises galaxies at higher redshift compared to their minimum scatter projection. The $z = 0$ RSZR and the local FMR are identical by construction, therefore the ratio for all three simulations at $z = 0$ is 1.0. In Illustris and EAGLE at $z \leq 2$ the scatter reduction by using a RSZR fit is less than 5% (within our uncertainty on α_{\min}). The relatively low decrease in the scatter implies that the RSZR and local FMR are functionally similar at these low redshifts. The scatter reduction at $z \geq 3$, however, is $\geq 10\%$. Both Illustris and EAGLE have monotonically decreasing ratios of scatter in the high- z regime out to a 20% decrease in Illustris and nearly 40% in EAGLE. The scatter reduction stays roughly constant in TNG at just over 10% at $z > 0$. This roughly constant scatter reduction lends further credence to the idea that there is little redshift evolution of the FMR in TNG at any redshift *but* $z = 0$. The decrease in scatter when using the RSZR indicates that high redshift galaxies are different from the low redshift systems. The local FMR clearly does not effectively characterise higher redshift galaxies. This marked shift in efficacy of the local FMR indicates that there is some time evolution within the FMR past $z \geq 3$.

5.1.2 Removing high redshift offsets

Local FMRs are constructed to minimize the scatter at $z = 0$ and are *completely* agnostic to whether the residuals are centered around zero at any other redshift. This definition is in line with the strong FMR hypothesis (see Section 3.2). In taking the strong FMR hypothesis we are explicitly stating that there should be no high redshift offsets. However, as we show in Section 4.2.1, systematic offsets from the local FMR exist in high redshift galaxy populations of Illustris, TNG, and EAGLE. Here we offer one solution for the offsets from the FMR by considering a modification to the definition of the local FMR.

We define a modified local FMR where α_{local} is determined, by definition, at only $z = 0$ but the regression now includes high redshift galaxies. Figure 7 shows this modification for EAGLE (see Figures B4 and B3 for TNG and Illustris versions). The only change between Figures 4 and 7 are the slope and intercept of the FMR regression (solid black lines on all panels of both Figures).

We find that by considering high- z galaxies in the regression the slope steepens in EAGLE and TNG and flattens slightly in Illustris. The net effect of the modified slope is to more closely pass through the distributions of high redshift galaxies (as can be seen in the nine panels on the right of Figures 7, B3, and B4).

A summary of the change in offsets by using the altered local FMR definition is provided in Figure 8. We find that the magnitude of the offsets is significantly reduced at high redshift across all three simulations. In fact, the average offsets are near 0.0 for all redshift bins in Illustris and EAGLE. From the elimination of offsets in EAGLE and

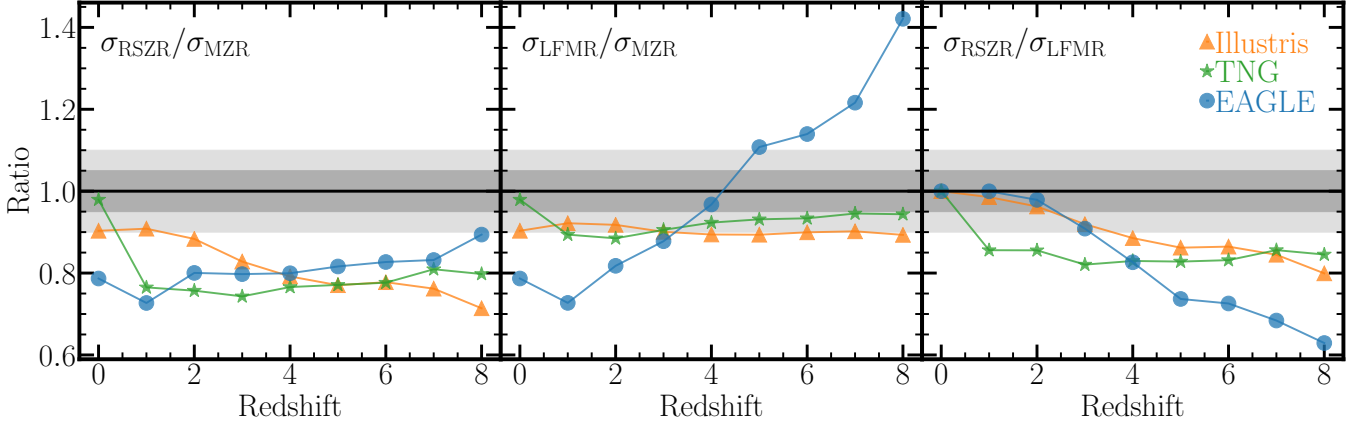


Figure 6. Reduction in scatter using RSZR versus MZR, Local FMR vs MZR, and RSZR versus Local FMR. *Left:* the scatter about the $\mu_{\alpha ZR}$ by fitting at each redshift individually (σ_{RSZR}) divided by the scatter in the MZR at each redshift (σ_{MZR}) as a function of redshift. The dark and light gray shaded regions (in all panels) represent 5% and 10% variations, respectively, of each ratio. *Centre:* Same as left, but now the numerator is the scatter about the $\mu_{\alpha ZR}$ evaluated in each redshift bin with a $z=0$ FMR fit (σ_{LFMR}). *Right:* Previous two panels divided by each other. This is the reduction in scatter in the relationship by fitting each redshift independently (σ_{RSZR}) divided by using a local FMR fit (σ_{LFMR}).

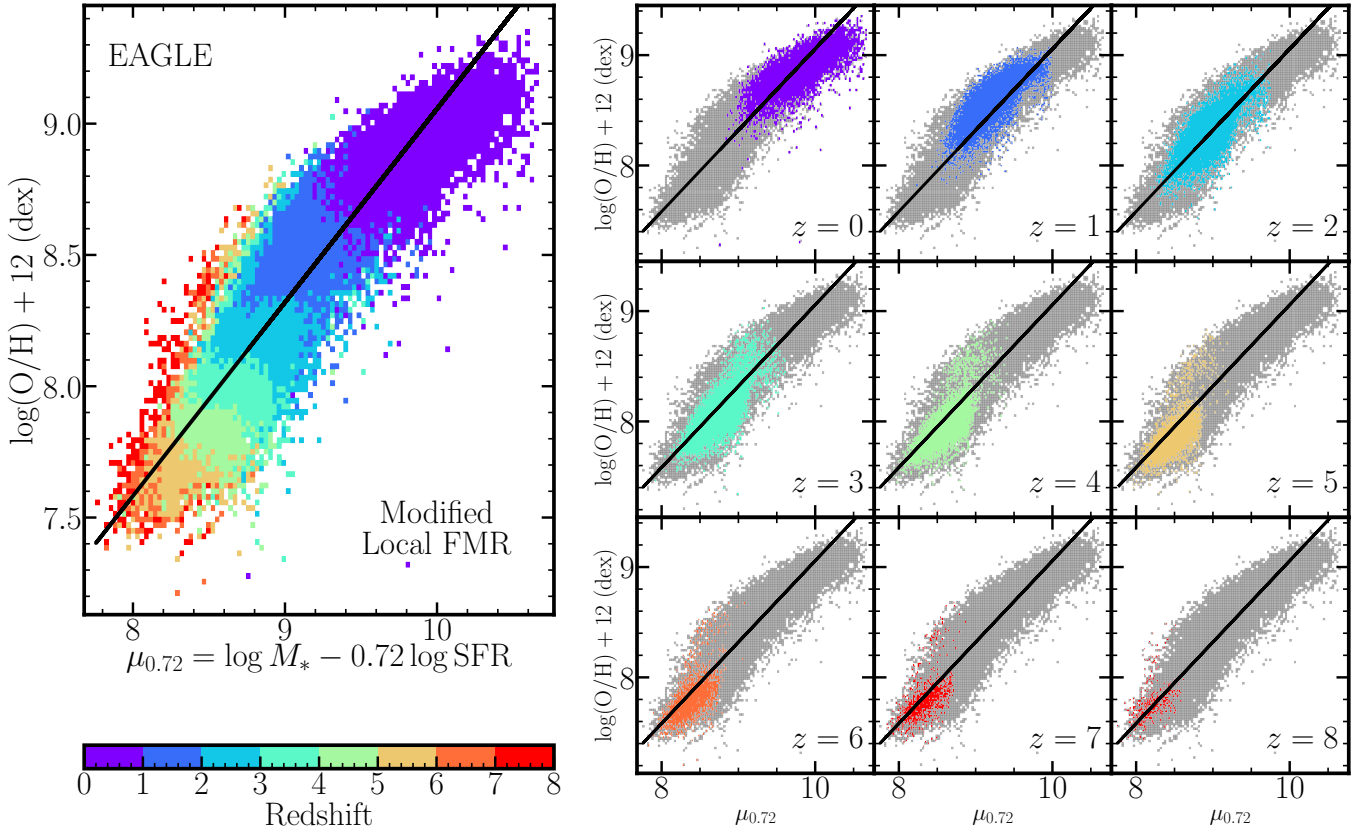


Figure 7. The modified local FMR (α_{\min} determined at $z=0$ and regression fit on $z=0-8$ galaxies) for EAGLE. *Left:* Local FMR with α_{\min} determined at $z=0$, but with a regression fit including higher redshift data from $z=0-8$ in EAGLE (same colour-coding as Figure 4). The solid black line is a linear-least squares regression of all data points. *Right:* Each redshift individually with the modified local FMR overplotted, same colour-scheme as left panel. The gray background distribution is the left panel without colour, for reference.

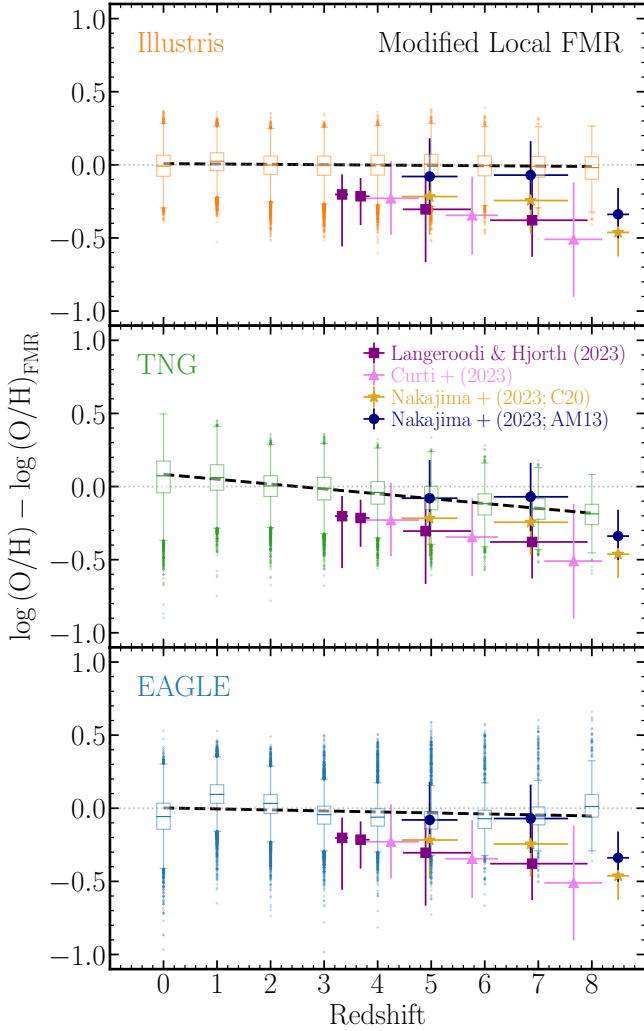


Figure 8. How do offsets change when considering a modified local FMR? Offsets from the modified local FMR (α_{\min} determined at $z = 0$, regression fit on $z = 0 - 8$ galaxies) for Illustris (top; orange), TNG (middle; green), and EAGLE (center; blue). Similar to Figure 5, the box plots are the full distribution of offsets. The dashed black line is a linear regression through the means of the offsets. Additionally, we overplot data from recent *JWST* observations, which compare to a (non-modified) local FMR (purple squares, Langeroodi & Hjorth 2023; pink triangles, Curti et al. 2023; gold stars and dark blue circles, Nakajima et al. 2023).

Illustris we see that FMR offsets are sensitive to the considerations (or lack thereof) for high redshift galaxies when fitting the FMR. For TNG, however, the modification gives rise to an increase in offsets at low redshift and only modestly reduces the offsets at high redshift. One possible explanation for the increase in offsets at low redshift could be the large difference in α_{\min} values from $z = 0$ to $z \geq 1$ (as shown in Figure 3). The scatter about the $z = 0$ MZR in TNG has a fairly weak dependence on SFR (see left panel of Figure 6). The lack of dependence is felt strongly in the local FMR parameterisation owing to the $z = 0$ focus placed on it and may be further compounded in this modified version of the local FMR. What is likely happening here is that the $z = 0$ calibrated α_{\min} is so different from what is required to minimize the scatter in the higher redshifts that the distribution of galaxies in μ_{α} -metallicity space is significantly different from the minimum scatter projection (i.e., RSZR at that redshift). The modi-

fied local FMR is consequently “penalized” with a weak relationship at $z = 0$ being enforced on high redshifts. Fitting the larger-scatter high redshift populations (i) creates a worse fit for $z = 0$, and (ii) is not well-posed for the high redshift distributions. We believe that the penalty that the modified local FMR pays manifests itself in the existence of offsets at low- z in TNG.

It should be noted that most of the distributions of galaxies shown in the right-hand panels of Figure 7 are not “minimum scatter projections” (see previous section). The scatter about the modified local FMR is very similar to that of the local FMR; the distribution of points remains the same since α_{local} is the same. The distribution of galaxies has increased scatter compared to the traditional local FMR if α_{RSZR} at a given redshift is not the same as α_{RSZR} at $z = 0$ (see Figure 6). The additional scatter in the projections therefore comes from α_{RSZR} varying as a function of redshift. The net effect of the increased scatter in the distributions is to skew the least squares regression towards the largest residual galaxies. Large deviations are penalised significantly by the χ^2 minimisation of the least-squares regression. The result is a regression that is difficult to interpret. Are offsets from this regression due to a sub-optimal projection into 2D or are they changes in the physics driving scatter? We simply shift our uncertainty into α_{RSZR} variations in eliminating high redshift offsets rather than meaningfully improve the local FMR.

The underlying basis for the FMR is an assertion that not only do variations in the SFRs (or gas masses, or gas fractions) correlate with changes in the metallicity of $z = 0$ galaxies, but that the redshift evolution of the normalization of the MZR can be attributed to changes in the SFRs (or gas masses, or gas fractions) at higher redshifts. This is a powerful concept, which implies that the same physical mechanisms that drive scatter in the MZR at $z = 0$ also play a central role in determining the metallicity of high redshift galaxy populations. However, not only do recent *JWST* findings challenge this conclusion, in this paper we also find that neither Illustris, TNG, nor EAGLE agree with this conclusion. To this end, we have two key findings: (i) there is non-negligible in α_{RSZR} (which should not be the case for an FMR), and (ii) high redshift simulated galaxy populations do not fall along the locally defined FMR. We can somewhat remedy the second of these two points by defining a modified FMR, whereby we fix alpha locally (i.e. with $z = 0$ data, as is traditional) but where the regression that defines the FMR plane is defined while considering galaxies across all redshift bins. Unsurprisingly, this does remove/reduce the high-redshift offsets, but does so only by somewhat enhancing the magnitude of the scatter for certain other redshifts. Calibrating a potentially redshift-invariant plane with only the local galaxies may not provide adequate constraints for galaxies across a wide range of time.

5.2 Evaluating the presented relations

As we have shown, there are two distinct features that arise when calibrating the FMR: (i) variations in α_{\min} , which are indicative of the strength of the correlated scatter changing with time (Section 4.1), and (ii) offsets in high-redshift galaxy populations (Section 4.2.1). Each of these features can be rectified, the former by fitting each redshift individually (i.e., RSZR) and the latter by calibrating the FMR regression with high redshift galaxy populations (i.e., modified local FMR). In this section we address the practicality of each of these methods, as well as discuss their limitations.

5.2.1 RSZR

The RSZR effectively minimizes the scatter by considering each redshift independently (especially in comparison to the local FMR at high z ; see Figure 6). Herein lies the advantage of using the RSZR: by fitting the scatter about each redshift independently, a clear-cut metric for the strength of correlated scatter arises that is completely independent of the evolution of the normalisation of the MZR. Independence from other redshift populations removes the possibility of conflating evolution of the normalisation of the MZR with evolution of the scatter. At the same time, in fitting each redshift independently, we lose all potential for information regarding the evolution of the normalisation. The RSZR only truly addresses one half of the goal of the FMR and therefore cannot be considered an “FMR” (as illustrated in Figure 2). Yet, the RSZR allows us to probe the fundamental nature of the FMR by providing a diagnostic by which the potential redshift evolution seen in the FMR can be decoupled. Any evolution *must* be driven by the evolution of the normalisation of the MZR if α_{\min} were constant with redshift.

One challenge of an observational RSZR analysis is the amount of data available. Lower redshift galaxy populations are well sampled, but at higher redshift sampling becomes more difficult. Yet, the most significant evolution in α_{RSZR} happens in these highest redshift populations (Figure 3). More complete samples of galaxy populations at these early times are therefore required in order to undergo any RSZR analysis to detect significant deviations from the $z = 0$ α_{RSZR} values.

5.2.2 Local FMR

The key advantage of the local FMR is its observability. Redshift zero far and away offers the most fully sampled parameter space of galaxies of any redshift with millions of galaxies in the catalogs of local surveys (e.g., SDSS, Abazajian et al. 2009). Calibrating an FMR using the abundant local galaxy population is a natural choice. Yet this low redshift calibrated FMR produces systematic offsets at high redshift (as we show in Section 4.2.1). The offsets at high redshift indeed indicate some redshift evolution from the $z = 0$ FMR, but they are difficult to interpret. Do the offsets indicate that the FMR is a state of equilibrium achieved by galaxies at $z \sim 3$ (e.g., Langeroodi & Hjorth 2023) or do they indicate that the $z = 0$ calibration is not valid across all redshifts (e.g., Curti et al. 2023)? Furthermore, high redshift offsets can be reduced or even removed entirely by introducing higher redshift galaxies into the FMR regression – even without considerations for α_{\min} at the higher redshifts. Do the offsets simply signal that when fitting the FMR we need to include higher redshift galaxies? It is difficult to answer any of these questions concretely; however, it is clear that the locally derived FMR regression is not a perfect fit for high redshift galaxy populations.

Another downside of the local FMR is that we suppress any variations of α_{\min} as a function of redshift. As a consequence, the local FMR also does not optimally reduce scatter across redshift (as shown in Section 5.1.1). Parameterising with sub-optimal values of α_{\min} changes the distribution of galaxies within μ_{α} -metallicity space and impacts both the offsets (Figure 8) and scatter (Figure 6).

5.2.3 Modified Local FMR

The modified local FMR is qualitatively similar to the local FMR in terms of advantages and disadvantages. The chosen modification does help alleviate offsets at high redshift; however, α_{\min} variations

are still marginalised over. Distributions of galaxies are unchanged, since α_{\min} is held fixed, therefore the scatter about the relation is unchanged. While alleviating one tension of the FMR model, the modified local FMR does not help the sub-optimal fitting of high redshift galaxy populations.

One particular quirk of the modified local FMR can be seen if α_{\min} variations are rapid enough at low redshift, as in TNG. Distributions of galaxies in μ_{α} -metallicity space have significant differences from the minimum scatter distribution (i.e., that from the RSZR) in TNG. Offsets from the modified local FMR therefore persist in TNG (discussed in full in Section 5.1.2). A modified version of the local FMR may be able to indicate large α_{\min} variations at low redshift, independent of an RSZR analysis.

5.2.4 Global FMR

Though not presented in this work, one could also imagine changing the calibration of the FMR to *entirely* include higher redshift galaxies (not just the regression). This relationship is the global FMR. The global FMR is qualitatively similar to the modified version of the local FMR. The main difference between global FMR and modified local FMR is that the α_{global} determination contains data across all redshifts (whereas α_{local} is only $z = 0$).

Many of the same issues are present in the global FMR as in the modified local FMR. Most obviously, α_{\min} variations are entirely ignored. The global FMR, however, is worse in its (mis)treatment of α variations. α_{global} may not produce a minimum scatter projection at any individual redshift whereas the local FMR at least produces the $z = 0$ minimum scatter. It is therefore likely that the scatter about the global FMR is similar (if not worse) than the local FMR. As an extreme example, if the residual correlation at each redshift was reversed (i.e., higher metallicity is higher gas content) it is possible that the “correct” residual correlation may be recovered (higher metallicity is lower gas content) in determining α_{global} based solely on evolution of the normalisation. The global FMR regression is similarly plagued. The regression is difficult to interpret since many (potentially all) of the individual redshifts are not minimum scatter projections. Similar questions from before arise: Are any offsets caused by a change in physics over time or are they an artifact of fitting over the “wrong” distributions? For these reasons, we choose not to present a global FMR in this work.

6 CONCLUSIONS

We select central star forming galaxies with stellar mass $8.0 < \log(M_* [M_{\odot}]) < 10.5$ with gas mass $\log(M_{\text{gas}} [M_{\odot}]) > 8.5$ from $z = 0 - 8$ in the cosmological simulations Illustris, IllustrisTNG, and EAGLE. We investigate the extent to which the M10 parameterisation of the fundamental metallicity relation (FMR; Equation 1) holds. The parameter of merit in the M10 parameterisation is α_{\min} , which traditionally is understood as a parameter to minimize scatter about the MZR. Physically, α_{\min} sets a projection direction of the mass-metallicity-SFR space to a 2D space with minimal scatter. Many observational studies have claimed that this projection direction does not evolve with redshift (Mannucci et al. 2010; Cresci et al. 2019). This potentially indicates that the FMR can predict the evolution of both the scatter about the MZR and the normalisation of the MZR.

We define both a strong and weak FMR hypothesis. The strong FMR hypothesis states the the M10 parameterisation can describe both the scatter and normalisation of the MZR at the same time. The

weak FMR hypothesis states that the scatter and normalisation are disjoint, but the scatter does not evolve with redshift.

We deliberately define relationships within the **M10** framework (Section 3; Figure 2) to test the strong and weak FMR hypotheses. The analysis in this work focuses on three relationships within this framework. The first is the reduced scatter metallicity relation (RSZR). The RSZR determines the minimum scatter projection at each redshift independently. We stress that the RSZR is *not* a version of the fundamental metallicity relation. The other relationship we examine in this work is the local FMR, wherein α_{\min} is determined only using $z = 0$ galaxies.

Our conclusions are as follows:

- We find that there is non-negligible evolution of the scatter about the MZR as a function of redshift (Figure 3) by using the RSZR. This result suggests that the weak FMR hypothesis does not hold in Illustris, TNG, and EAGLE.
- We examine a local FMR (Figure 4), wherein α_{\min} and the regression are fit only on $z = 0$ galaxies (similar to typical observational studies, e.g., **M10**; Andrews & Martini 2013; Curti et al. 2020). We find offsets from this locally-defined FMR in each of the three simulations at high redshift (Figure 5). Offsets at high redshift in simulations echo recent *JWST* studies (Curti et al. 2023; Langeroodi & Hjorth 2023; Nakajima et al. 2023). While Illustris galaxies are more metal *rich* than high- z predictions, the offsets in TNG and EAGLE agree remarkably well with these observations at $z \gtrsim 3$.
- We find that the reduced scatter metallicity relation (RSZR; α_{\min} determined at each redshift independently) fits reduce scatter around 10 – 30% compared to the the MZR (left panel of Figure 6). The local FMR also reduces the scatter compared to the MZR, albeit to a lesser extent than the RSZR fits. At high- z in EAGLE, however, using the local FMR fit actually *increases* scatter compared to the MZR (centre panel of Figure 6). Overall, we find that at $z \gtrsim 3$ fitting galaxies with an RSZR can reduce scatter $\sim 5 - 40\%$ more than using the local FMR (right panel of Figure 6).
- By considering a modification to the local FMR (Figure 7) wherein the regression includes high redshift galaxies, we find that the systematic offsets can be removed entirely in Illustris and EAGLE (Figure 8, top and bottom, respectively). The offsets are reduced in TNG at high redshift, but low redshift offsets appear (Figure 8 centre panel). The modified local FMR, by definition, does *not* do any better fitting the scatter. We therefore simply shift the error to generalizing over α_{\min} variations by alleviating the tension of high redshift offsets.

Obtaining one relationship that describes the metal evolution of all galaxies across time is an ambitious goal. It is worth appreciating how reasonably well a simple linear combination of two parameters can begin to achieve that goal. Yet it is not perfect. The relationships employed in this work (RSZR and local FMR) show that Illustris, TNG, and EAGLE indicate deviations from both the strong and weak FMR hypotheses. We conclude therefore that (according to the **M10** parameterisation) the FMR evolves in these simulations.

ACKNOWLEDGEMENTS

AMG acknowledges Carol, Kate, and Kelly Garcia for assistance in the design of Figure 2. We acknowledge the Virgo Consortium for making their simulation data available. The EAGLE simulations were performed using the DiRAC-2 facility at Durham, managed by the ICC, and the PRACE facility Curie based in France at TGCC, CEA, Bruyères-le-Châtel.

DATA AVAILABILITY

The data that support the findings of this study are available upon request from the corresponding author. Data from Illustris and IllustrisTNG is publicly available on each project's respective website. Illustris: <https://www.illustris-project.org/data/> and IllustrisTNG: <https://www.tng-project.org/data/>. Similarly, data products from the EAGLE simulations are available for public download via the Virgo consortium's website: <https://icc.dur.ac.uk/Eagle/database.php>

REFERENCES

- Abazajian K. N., et al., 2009, *ApJS*, **182**, 543
- Andrews B. H., Martini P., 2013, *ApJ*, **765**, 140
- Belli S., Jones T., Ellis R. S., Richard J., 2013, *ApJ*, **772**, 141
- Blanc G. A., Lu Y., Benson A., Katsianis A., Barraza M., 2019, *ApJ*, **877**, 6
- Bothwell M. S., Maiolino R., Kennicutt R., Cresci G., Mannucci F., Marconi A., Ciccone C., 2013, *MNRAS*, **433**, 1425
- Bothwell M. S., Maiolino R., Peng Y., Ciccone C., Griffith H., Wagg J., 2016, *MNRAS*, **455**, 1156
- Chabrier G., 2003, *PASP*, **115**, 763
- Crain R. A., et al., 2015, *MNRAS*, **450**, 1937
- Cresci G., Mannucci F., Curti M., 2019, *A&A*, **627**, A42
- Curti M., Mannucci F., Cresci G., Maiolino R., 2020, *MNRAS*, **491**, 944
- Curti M., et al., 2023, *arXiv e-prints*, p. [arXiv:2304.08516](https://arxiv.org/abs/2304.08516)
- Dalcanton J. J., 2007, *ApJ*, **658**, 941
- Davis M., Efstathiou G., Frenk C. S., White S. D. M., 1985, *ApJ*, **292**, 371
- De Rossi M. E., Bower R. G., Font A. S., Schaye J., Theuns T., 2017, *MNRAS*, **472**, 3354
- De Rossi M. E., Bower R. G., Font A. S., Schaye T., 2018, *Boletín de la Asociación Argentina de Astronomía La Plata Argentina*, **60**, 121
- Dolag K., Borgani S., Murante G., Springel V., 2009, *MNRAS*, **399**, 497
- Donnari M., et al., 2019, *MNRAS*, **485**, 4817
- Ellison S. L., Patton D. R., Simard L., McConnachie A. W., 2008, *ApJ*, **672**, L107
- Elmegreen B. G., 1999, *ApJ*, **527**, 266
- Fontanot F., et al., 2021, *MNRAS*, **504**, 4481
- Garcia A. M., et al., 2023, *MNRAS*, **519**, 4716
- Garcia A. M., et al., In Preparation, In Preparation,
- Genel S., et al., 2014, *MNRAS*, **445**, 175
- Heintz K. E., et al., 2022, *arXiv e-prints*, p. [arXiv:2212.02890](https://arxiv.org/abs/2212.02890)
- Hemler Z. S., et al., 2021, *MNRAS*, **506**, 3024
- Kewley L. J., Nicholls D. C., Sutherland R. S., 2019, *ARA&A*, **57**, 511
- Koeppen J., 1994, *A&A*, **281**, 26
- Lacey C. G., Fall S. M., 1985, *ApJ*, **290**, 154
- Langeroodi D., Hjorth J., 2023, *arXiv e-prints*, p. [arXiv:2307.06336](https://arxiv.org/abs/2307.06336)
- Langeroodi D., et al., 2022, *arXiv e-prints*, p. [arXiv:2212.02491](https://arxiv.org/abs/2212.02491)
- Lara-López M. A., et al., 2010, *A&A*, **521**, L53
- Lee H., Skillman E. D., Cannon J. M., Jackson D. C., Gehrz R. D., Polomski E. F., Woodward C. E., 2006, *ApJ*, **647**, 970
- Maiolino R., et al., 2008, *A&A*, **488**, 463
- Mannucci F., Cresci G., Maiolino R., Marconi A., Gnerucci A., 2010, *MNRAS*, **408**, 2115
- Marinacci F., et al., 2018, *MNRAS*, **480**, 5113
- McAlpine S., et al., 2016, *Astronomy and Computing*, **15**, 72
- Naiman J. P., et al., 2018, *MNRAS*, **477**, 1206
- Nakajima K., Ouchi M., Isobe Y., Harikane Y., Zhang Y., Ono Y., Umeda H., Oguri M., 2023, *arXiv e-prints*, p. [arXiv:2301.12825](https://arxiv.org/abs/2301.12825)
- Nelson D., et al., 2018, *MNRAS*, **475**, 624
- Nelson D., et al., 2019a, *Computational Astrophysics and Cosmology*, **6**, 2
- Nelson D., et al., 2019b, *MNRAS*, **490**, 3234
- Nelson E. J., et al., 2021, *MNRAS*, **508**, 219
- Onodera M., et al., 2016, *ApJ*, **822**, 42
- Pillepich A., et al., 2018a, *MNRAS*, **473**, 4077
- Pillepich A., et al., 2018b, *MNRAS*, **475**, 648
- Pillepich A., et al., 2019, *MNRAS*, **490**, 3196

- Salim S., Lee J. C., Davé R., Dickinson M., 2015, *ApJ*, **808**, 25
- Sanders R. L., et al., 2018, *ApJ*, **858**, 99
- Sanders R. L., et al., 2021, *ApJ*, **914**, 19
- Savaglio S., et al., 2005, *ApJ*, **635**, 260
- Schaye J., 2004, *ApJ*, **609**, 667
- Schaye J., Dalla Vecchia C., 2008, *MNRAS*, **383**, 1210
- Schaye J., et al., 2015, *MNRAS*, **446**, 521
- Somerville R. S., Davé R., 2015, *ARA&A*, **53**, 51
- Springel V., 2005, *MNRAS*, **364**, 1105
- Springel V., 2010, *MNRAS*, **401**, 791
- Springel V., Hernquist L., 2003, *MNRAS*, **339**, 289
- Springel V., White M., Hernquist L., 2001, *ApJ*, **549**, 681
- Springel V., et al., 2018, *MNRAS*, **475**, 676
- Torrey P., Vogelsberger M., Genel S., Sijacki D., Springel V., Hernquist L., 2014, *MNRAS*, **438**, 1985
- Torrey P., et al., 2018, *MNRAS*, **477**, L16
- Tremonti C. A., et al., 2004, *ApJ*, **613**, 898
- Troncoso P., et al., 2014, *A&A*, **563**, A58
- Vogelsberger M., Genel S., Sijacki D., Torrey P., Springel V., Hernquist L., 2013, *MNRAS*, **436**, 3031
- Vogelsberger M., et al., 2014a, *MNRAS*, **444**, 1518
- Vogelsberger M., et al., 2014b, *Nature*, **509**, 177
- Weinberger R., et al., 2017, *MNRAS*, **465**, 3291
- Wiersma R. P. C., Schaye J., Theuns T., Dalla Vecchia C., Tornatore L., 2009, *MNRAS*, **399**, 574
- Yang N., Scholte D., Saintonge A., 2022, *arXiv e-prints*, p. [arXiv:2212.10657](https://arxiv.org/abs/2212.10657)
- Zahid H. J., Kewley L. J., Bresolin F., 2011, *ApJ*, **730**, 137

APPENDIX A: HIGHER ORDER POLYNOMIAL

M10 determined residuals in the scatter about a fourth-order polynomial instead of a linear regression. This practice is not consistent through all works using the μ_α 2D projection of the FMR, however. For example, recent *JWST* observational papers (e.g., [Nakajima et al. 2023](#); [Langeroodi & Hjorth 2023](#)) adopt a linear regression definition of the FMR from [Andrews & Martini \(2013\)](#). We define $\alpha_{\text{fourth-order}}$ as α_{RSZR} but now fitting the FMR regression with a fourth order polynomial. We also specify α_{linear} for α_{RSZR} using a linear regression for clarity. Comparing α_{linear} and $\alpha_{\text{fourth-order}}$ will test if the order of the regression is important in α_{min} determinations. We show that using a linear regression does not significantly change the projection of least scatter in Figure A1. We find that by using a fourth-order polynomial does not change α_{RSZR} at any redshift in Illustris and EAGLE by more than 5%. Only two α_{RSZR} values are changed by more than 5% in TNG ($z = 0$ by 15% and $z = 3$ by 7%). Fitting a fourth-order polynomial at $z = 0$ in TNG shows a decreased dependence on SFR compared to the linear regression. The uncertainty on α_{RSZR} ($z = 0$) in TNG extends down to 0 (see Table 1); therefore, a smaller α_{RSZR} value is unsurprising when using a slightly different regression.

APPENDIX B: ILLUSTRIS AND TNG VERSIONS OF FIGURES 4 AND 7

We chose to only present EAGLE versions of Figures 4 and 7 in the main body of the text for clarity. Each simulation has slightly different behaviour, however. We therefore append the Illustris and TNG versions of Figure 4 as Figures B1 and B2, respectively. We also append Illustris and TNG version of the modified local FMR (Figure 7) in Figures B3 and B4, respectively.

This paper has been typeset from a \LaTeX file prepared by the author.

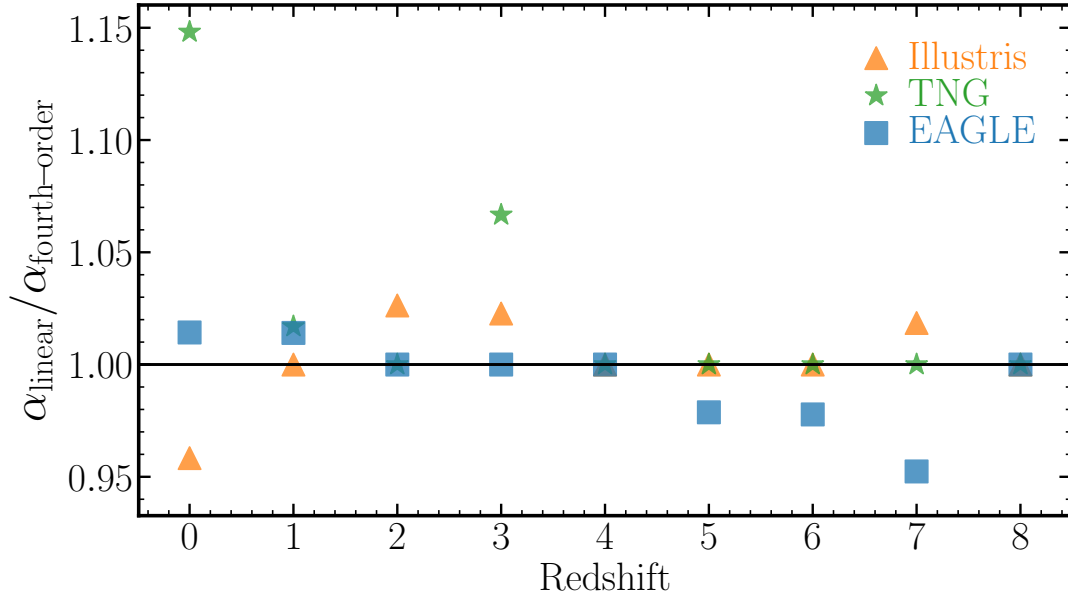


Figure A1. Ratio of minimum scatter projection parameter using a linear regression (α_{linear}) and a fourth-order polynomial regression ($\alpha_{\text{fourth-order}}$) as a function of redshift for Illustris (orange triangles), TNG (green stars), and EAGLE (blue squares).

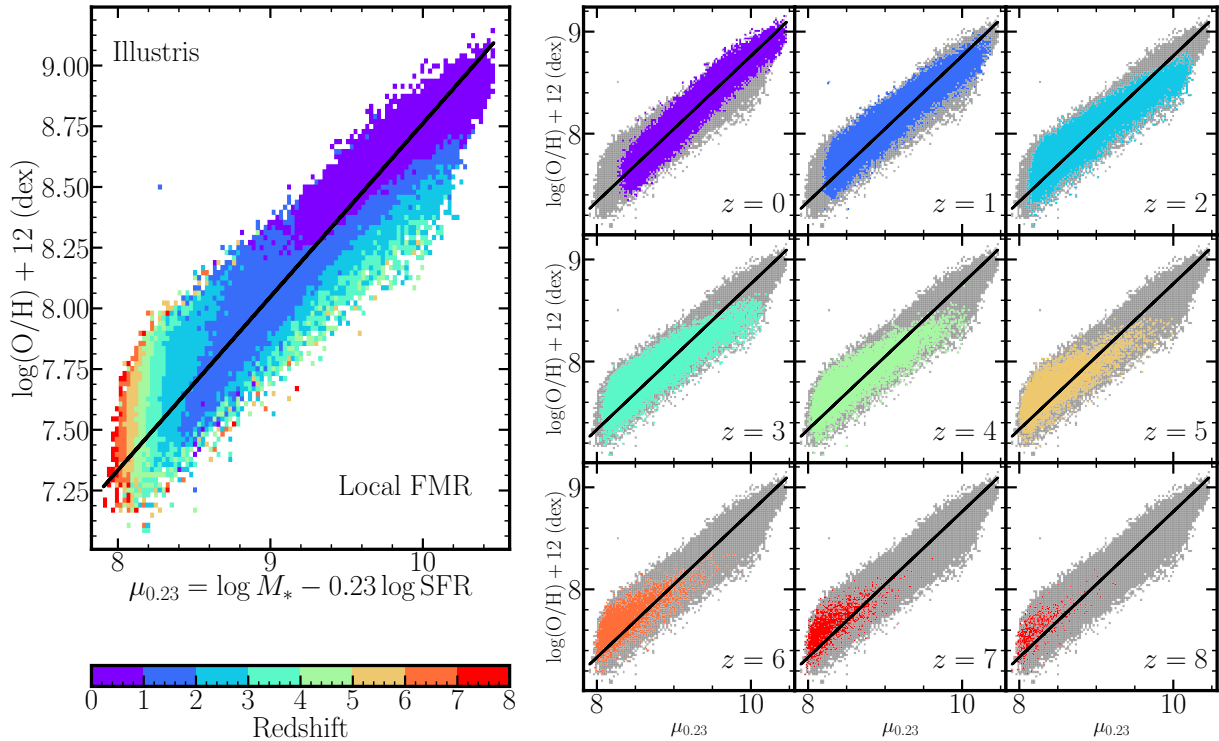


Figure B1. Same as Figure 4, but for Illustris

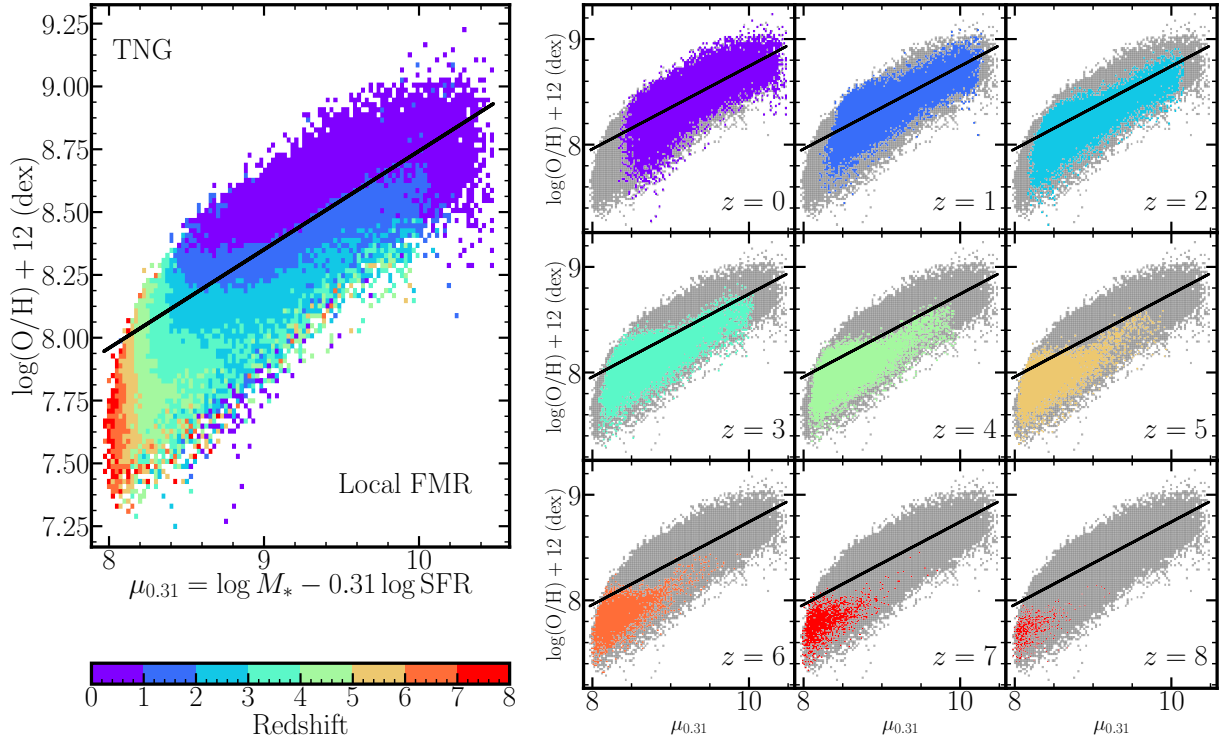


Figure B2. Same as Figure 4, but for TNG

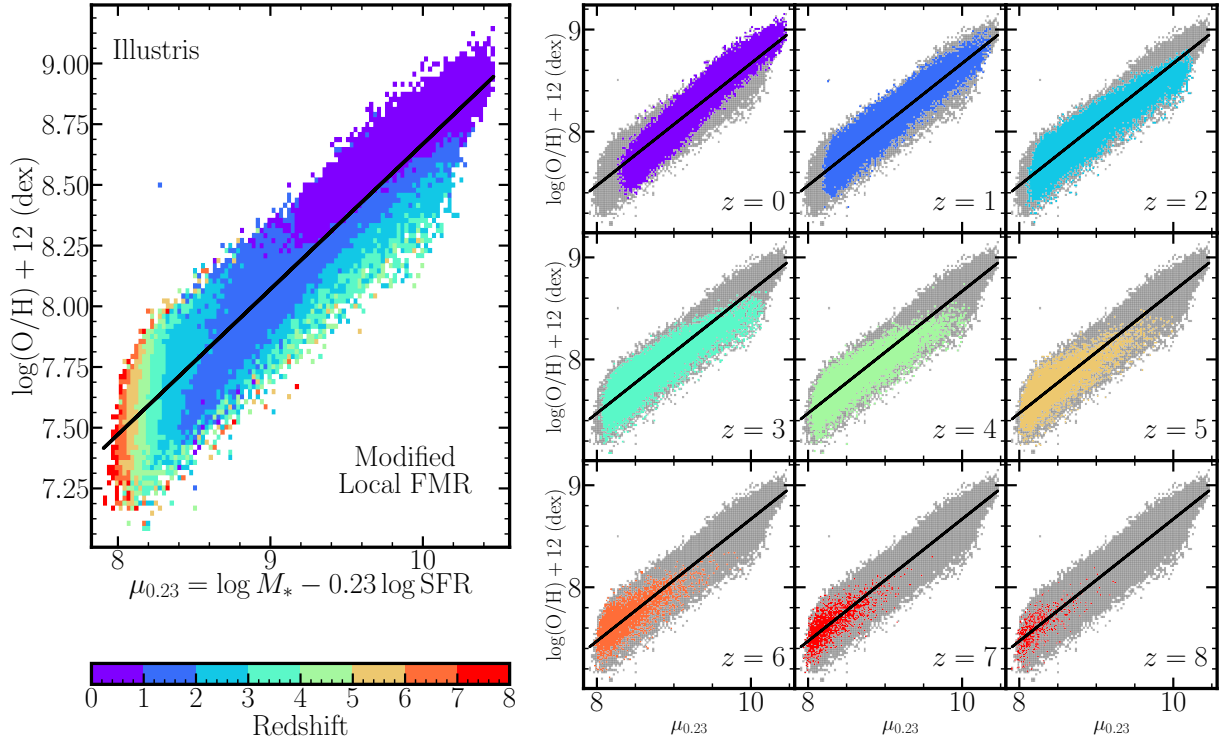
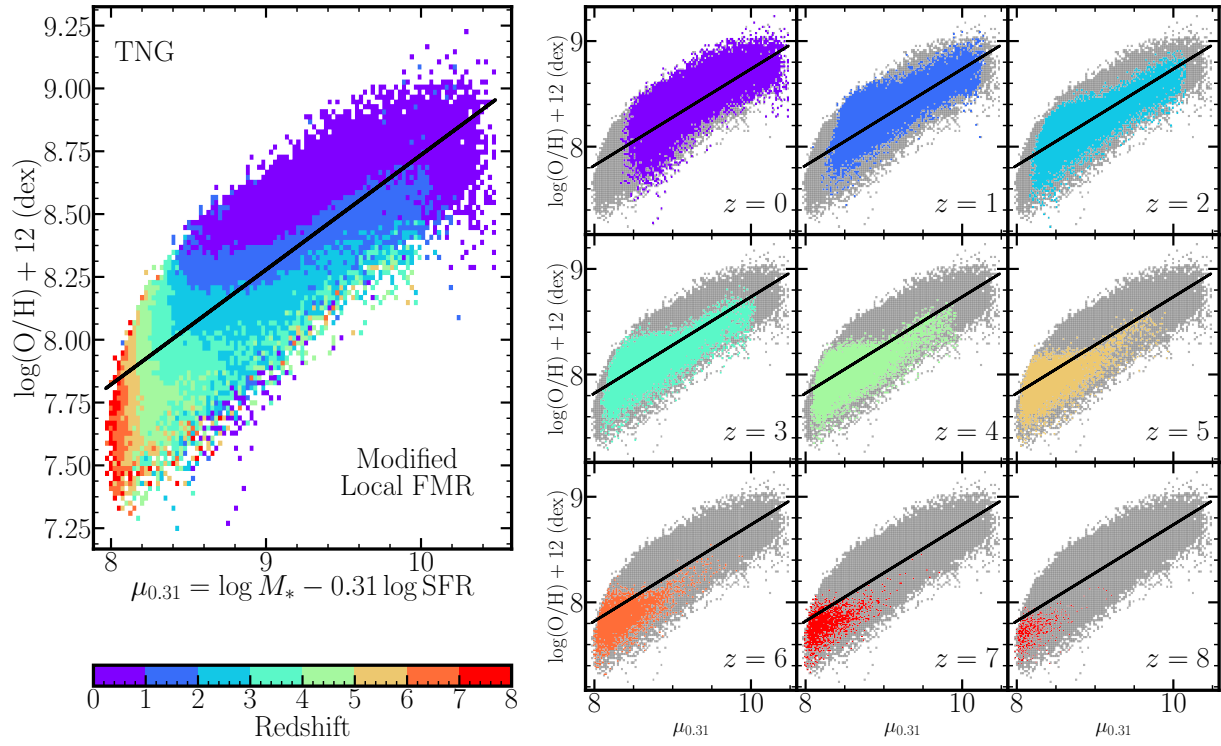


Figure B3. Same as Figure 7, but for Illustris

**Figure B4.** Same as Figure 7, but for TNG